SRTTU
Journal of Computational and Applied Research in Mechanical Engineering
jcarme.sru.ac.ir
JCARME
ISSN: 2228-7922

Research paper

Discrete phase numerical study of the effects of nanofluid on the performance characteristics of water chiller

Atie Farrokh and Miralam Mahdi*

[a] *Faculty of Mechanical Engineering, Shahid Rajaee Teacher Training University, Tehran, IRAN*

Article info:

Article history:

Received: 00/00/0000
Revised: 00/00/0018
Accepted: 00/00/0000
Online: 00/00/0000

Keywords:
Nanoparticles,
Chiller,
Evaporator,
Discrete phase,
Heat transfer.

***Corresponding author:**
M.mahdi@sru.ac.ir

Abstract

Chillers are among the most widely used air-conditioning systems, and improving their thermal performance can significantly reduce energy consumption. In the present study, the effects of Al_2O_3/water and Al_2O_3–TiO_2/water nanofluids on the performance characteristics of a shell-and-tube chiller evaporator were numerically investigated using an Eulerian-Lagrangian Discrete Phase Model (DPM). The influences of nanoparticle volume fraction, inlet fluid temperature, evaporator temperature, mass flow rate, and number of baffles were examined. Three evaporator configurations with 3, 5, and 7 baffles were considered. The results showed that increasing the number of baffles from 5 to 7 enhanced the overall heat transfer coefficient by 6.94%. The addition of Al_2O_3 nanoparticles increased the overall heat transfer coefficient by 5.8%, while the use of Al_2O_3–TiO_2 hybrid nanoparticles resulted in an enhancement of up to 8.8%. Analysis of the performance evaluation criterion (PEC) indicated that nanoparticle volume fractions up to 0.03 provide favorable thermal performance, with an optimum value around 0.02. The results also demonstrated a significant difference between the DPM and conventional single-phase predictions, with a relative discrepancy of approximately 68% in the estimated heat transfer enhancement under the investigated conditions. The findings confirm the potential of nanofluids, particularly hybrid nanofluids, for enhancing the thermal performance of shell-and-tube chiller evaporators.

1. Introduction

Nowadays, air conditioning is widely used in industrial, commercial, office, workshop, and residential sectors, and the chiller one of its most famous pieces of equipment. The chiller has received a lot of attention due to its wide application. In order to reduce the dimensions and size or increase the performance of the refrigeration cycle, measures have been taken, and studies have been done on different parts of the cycle in order to improve the economic and thermal efficiency of the cycle by increasing the amount of heat transfer, reducing the amount of work, or reducing the cost of maintenance. In this study, a case study of the evaporator, a part of the cycle that is related to the amount of heat transfer and the work of the evaporator pump,

has been discussed. Based on the results obtained from the studies conducted so far, the thermal performance coefficient of a shell and tube evaporator using mono aluminum oxide nanoparticles and Al_2O_3+TiO_2 hybrid nanoparticles in a water-base fluid has been investigated for three models of evaporator geometry. The investigated items are the secondary fluid flow rate, coolant and inlet temperature, nanoparticle concentration, and the number of evaporator baffles.

Atwal *et al.* [1] conducted a combined numerical and experimental analysis of heat transfer and pressure drop in a plate heat exchanger using Al_2O_3-MWCNT/water hybrid nanofluid at varying concentrations. Their findings revealed that the hybrid nanofluid outperformed conventional Al_2O_3/water nanofluid due to the superior thermal conductivity of multi-walled carbon nanotubes (MWCNTs). However, the study noted that the benefits of enhanced thermal conductivity must outweigh the increased viscosity for practical applications.

Rahman *et al.* [2] explored the impact of SWCNT/R-407c nano-refrigerant in a passive air conditioning system. By integrating energy-efficient features such as tree shading, double-glazed windows, and reflective roofing, the cooling load was reduced by 35%. Additionally, nanoparticle integration decreased compressor power consumption by 202.5 W, demonstrating significant energy savings.

Numerous studies have explored the effects of nanoparticles on enhancing the performance of refrigeration cycles and air conditioning systems. For instance, Jay Kumar *et al.*[3] investigated the effects of CuO, Al_2O_3, and ZnO nanoparticles on refrigeration cycle efficiency when mixed with R134a refrigerant. Their results indicated a 12.2% improvement in COP with CuO nanoparticles and a 3.42% increase with Al_2O_3, alongside energy consumption reductions of 1.39% and 0.6%, respectively.

According to Bhatad *et al.* [4] , nano-refrigerants enhance boiling and condensation heat transfer, improving system efficiency and reducing condenser size. Additionally, nanoparticles improve refrigerant-lubricant compatibility, extending compressor lifespan.

Vesconcillos *et al.* [5] examined SWCNT-based nanofluids in a cooling system's secondary loop, testing concentrations (0.2–0.5%), temperatures (30–40°C), and flow rates (40–80 kg/s). Their findings confirmed superior thermal performance compared to water.

Ahmed *et al.* [6] analyzed Al_2O_3/water and TiO_2/water nanofluids in a vapor compression system, observing that Al_2O_3/water delivered the highest COP (5.3% improvement) and fastest cooling. TiO_2/water showed a 4.1% lower condensation ratio.

In another study [7], compared Al_2O_3/water nanofluid (0.1–1% concentration) to pure water in a chilled water system. The nanofluid reduced cooling time and improved COP by 5–17%, with notable energy savings.

Meniri Menesh *et al.* [8] tested TiO_2/methanol nanofluid (3% concentration) in a heat pipe heat exchanger, achieving 26.1–43.7% energy savings in air conditioning.

Balaji *et al.* [9] used Al_2O_3 in ethylene glycol/water (30:70) within a coil-type heat exchanger, reporting a 49.32% COP increase and 12.2% lower power consumption at 0.75% concentration.

Another study [10] compared methanol and Ag/methanol nanofluids in HVAC reheating, showing 8.1–31.5% energy savings for methanol and 18–100% for Ag/methanol nanofluids.

Alavi *et al.* [11] summarized that nano-refrigerants can cut energy use while nano-lubricants boost heat transfer. Their integration improves both COP and cooling speed in refrigeration cycles.

Recent studies have continued to demonstrate the potential of nanofluids and hybrid nanofluids for enhancing heat transfer and improving the performance of HVAC and refrigeration systems. Myat *et al.* [12] reported that nanofluids can significantly improve thermal performance in HVAC&R applications while emphasizing the need for more detailed investigations of practical systems. Kalsi *et al.* [13] reviewed recent developments in hybrid nanofluids and concluded that hybrid nanoparticles generally provide superior thermal characteristics compared with mono nanofluids. Furthermore, Aliyu et *al.* [14] demonstrated the effectiveness of water-based hybrid nanofluids in improving

HVAC system performance. In addition, Ali *et al.* [15] showed that Eulerian-Lagrangian approaches can provide detailed information regarding nanoparticle transport, dispersion, and heat transfer mechanisms that cannot be directly captured by conventional mixture models. Despite these advances, limited attention has been devoted to the application of the DPM approach for investigating nanoparticle behavior and thermal-hydraulic performance in shell-and-tube chiller evaporators equipped with baffles.

Although several previous studies have investigated the application of nanofluids in refrigeration and air-conditioning systems, most of them have employed either experimental approaches or single-phase/mixed numerical models. In such approaches, the nanoparticle phase is usually assumed to be uniformly dispersed in the base fluid, and the individual particle transport, dispersion, and interaction with vortical structures cannot be directly evaluated. In contrast, the present study applies a Eulerian-Lagrangian Discrete Phase Model (DPM) to investigate the thermal and hydraulic behavior of Al_2O_3/water and Al_2O_3–TiO_2/water nanofluids in a shell-and-tube chiller evaporator. The main novelty of the present study lies in the application of the Eulerian-Lagrangian DPM approach to analyze nanoparticle motion, residence time, particle-vortex interactions behind baffles, and their effects on the overall heat transfer coefficient and performance evaluation criterion of a chiller evaporator. Moreover, the effects of baffle number, nanoparticle volume fraction, inlet temperature, and hybrid nanoparticle composition are simultaneously investigated to determine an appropriate operating range in which the heat transfer enhancement is greater than the pressure-drop penalty.

Most previous numerical studies on nanofluids in refrigeration and HVAC systems have employed single-phase or mixture models. Although these approaches provide acceptable predictions of overall thermal performance, they cannot directly capture nanoparticle trajectories, residence time, local accumulation, and interactions with recirculation zones. In shell-and-tube evaporators equipped with baffles, strong vortical structures are generated and significantly affect nanoparticle transport. Therefore, the Eulerian-Lagrangian Discrete Phase Model (DPM) was selected in the present study because it enables direct tracking of individual particles and provides a more detailed description of particle-fluid interactions within the complex evaporator geometry.

2. Equations

The principle of conservation of mass is a fundamental principle used in fluid mechanics. According to this principle, mass is neither produced nor destroyed, which is defined as the continuity equation for incompressible fluids as follows: [16]

$$div\left(\rho\vec{V}\right) = 0 \tag{1}$$

It is not possible to determine the mechanics of fluids by only having the continuity equation, and there is a need to state the principle of conservation of momentum or Newton's second law. The product of speed multiplied by mass is called the principle of the size of motion. Newton's second law states that the result of the forces acting on an object is equal to the net change in momentum.

$$\rho\frac{\partial\vec{V}}{\partial t} + div\left(\rho\vec{V}\vec{V}\right) = -gradP + \mu\left(\nabla^2\vec{V}\right) + S_v \tag{2}$$

Energy equation:

$$\rho C_p\frac{\partial T}{\partial t} + div\left(\rho\vec{V}C_pT\right) = k(\nabla^2T) + S_h \tag{3}$$

In the equations, V, P, T, and t represent the velocity, pressure, temperature, and time vectors, respectively. Additionally, μ, ρ, C_p, and k denote the viscosity, density, heat capacity, and thermal conductivity of water as the continuous phase, respectively. It is important to note S_v and S_h are source terms that account for the momentum exchange and energy interaction between particles and the fluid. These terms are defined as follows: [17]

$$S_v = \sum_{np} -\frac{m_p}{\delta V}\frac{dV_p}{dt} \quad (4)$$

$$S_h = \sum_{np} -\frac{m_p}{\delta V} c_p \frac{dT_p}{dt} \quad (5)$$

If t is time and V_p and $T_p$are speed and temperature of nanoparticles. In addition, m_p, np, and δV are the mass of nanoparticles, the number of particles in a cell volume, and the cell volume, respectively.

The trajectory of nanoparticles suspended in a fluid is determined using a force balance equation. The interaction forces between the fluid and particles include *drag force*, *Brownian force*, and *thermophoretic force*. The Brownian force arises from the random collisions of fluid molecules with the nanoparticles, while the thermophoretic force is caused by temperature gradients in the fluid.

For nanoparticles, the gravitational force is negligible, especially in cases where the particle diameter is as small as 10 nm. Even for particles larger than 50 nm, the gravitational force may have minimal impact and is therefore excluded from the calculations. The motion of the particle phase is governed by the following equation:[18]

$$\frac{dX_p}{dt} = V_p \quad (6)$$

$$\frac{dV_p}{dt} = F_D\left(V_f - V_p\right) + f_B + f_{th} \quad (7)$$

where the subscripts "f" and "p" represent fluid and particle, respectively. The first term on the right side of Eq. (7) is the drag force. Here, the Stokes-Cunningham drag force is used. Accordingly, [17]

$$F_D = \frac{18\mu_f}{d^2\rho_p C_c} \quad (8)$$

where $C_c$is the Cunningham correction defined by the following relation:

$$C_c = 1 + \frac{2\lambda}{d}\left[1.257 + 0.4e^{-(1.1d/2\lambda)}\right] \quad (9)$$

where λ is the mean free path of the fluid. The thermophoretic force is given as follows:

$$f_{th} = \frac{36\mu^2 C_s}{\rho_f \rho_p d_p^2 (1 + 3C_m Kn)} \times \frac{\left(k_f/k_p + C_t + Kn\right)}{\left(1 + 2k_f/k_p + 2C_t Kn\right)}\frac{\nabla T}{T} \quad (10)$$

where k_f, k_p, and Kn are thermal conductivity of fluid and nanoparticle and Knudsen number respectively. Also $C_m = 1.14$ ،$C_t = 2.18$, and $C_s = 1.17$.

In Eq. (7), the Brownian force is given as:

$$f_B = \varsigma\sqrt{\frac{\pi S_0}{\Delta t}} \quad (11)$$

Here, ς are independent Gaussian random numbers with zero mean and unit variance. In Eq. (11), S_0 is the spectral intensity of the Brownian force, which is evaluated as follows:

$$S_0 = \frac{216\nu K_B T}{\pi^2 \rho_f d_p^2 \left(\frac{\rho_p}{\rho_f}\right)^2 C_c} \quad (12)$$

Here, T, v, and K_B are the fluid's absolute temperature, kinematic viscosity, and Boltzmann's constant, respectively, and it is equal to $K_B = 1.38 \times 10e - 23\, J\, K^{-1}$.

First, in order to validate the DPM method as well as the simulation results, we use the flow model behind the step, which has experimental and simulation results available.

3. Validation

In this research, the behavior of the fluid, including nanoparticles, on the back-step flow model with the geometry shown in Fig. 1 has been investigated for validation. Specifications and dimensions are given in Table 1.

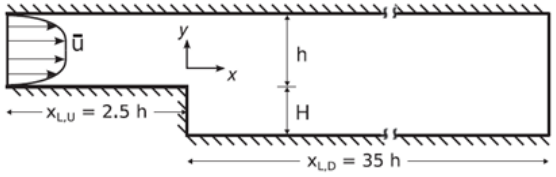

Fig. 1. Modeling geometry.

Table 1. Geometry dimensions of the model.

Step details		Channel details	
H	26.7 mm	h	40 mm
w/H	17:1	w	457 mm
		h/H	5:3

The modeling of the field has been done in two-dimensional and three-dimensional form, and its grid has been selected with a rectangular organization. The grid near the walls has been made finer and smaller in order to improve the quality of the investigation and the sensitivity of studying the changes in flow behavior near the wall. It has 31700 elements and 32147 nodes. By increasing the number of cells and reducing the size of the elements, no change has been observed in the simulation result, so the result is independent of the mesh. In the three-dimensional mode, the width of the channel is considered to be 2 mm, and for meshing the width, once it was meshed as one part and in the second mode as ten parts, the results of the first mode are better and, in terms of time and cost calculation, are more appropriate. In Fig. 2, you can see the meshing.

To check the independence of the solution and the results compared to the grid of three meshes with the number of cells 17252, 32147, and 78290 for the two-dimensional solution, the results for the vortex length are given in the table below for each grid. As can be seen in Table 2, by more than doubling the number of cells, in the third stage, not many changes were observed in the length of the vortex. Therefore, the grid with 32147 cells is selected to continue the solution. The material properties and boundary conditions are given in Table 3.

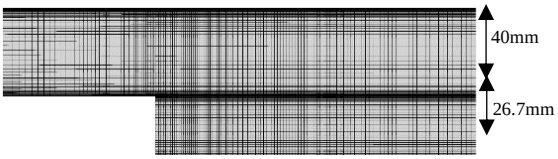

Fig. 2. Computational mesh used for the grid independence study, showing the mesh distribution in the computational domain.

Table 2. Independence from the grid

Percentage of changes	Vortex length (mm)	Number of cells
17252	0.2025	
32147	0.2036	0.54 %
78290	0.2041	0.24 %

Table 3. Material properties and boundary conditions.

Materials	Specifications	Unit	Quantity
Discrete phase	Density	kg/m^3	8800
	Particle diameter	μm	70
	Particle mass flow rate	kg/s	1.58×10^{-5}
	Injection speed	m/s	(10.5 0 0)
Continuous phase	Viscosity	m^2/s	1.5×10^{-6}
Inlet boundary condition	$U_{x,0}$	m/s	10.5
	$\bar{u}_{avg}$	m/s	(9.33 0 0)
	K	m^2/s^2	0.45
	ω	1/s	2800
Outlet boundary condition	$\bar{P}$	Pa	0
Wall boundary condition	$\bar{u}$	m/s	(0 0 0)

The mixing of particles with fluid and their diffusion due to turbulent structures are critical topics in numerous engineering applications. A deep understanding of the interaction between particles and turbulent fluid flows is essential for optimizing the performance of engineering systems. Turbulence is typically characterized by a wide range of eddy structures, spanning from the Kolmogorov scale to the characteristic length scale of the flow. These structures significantly influence the organized motion of particles within the fluid. In this section, the effects of vortices on particles with varying Stokes numbers are analyzed and compared.

The Stokes number (St) is defined as the ratio of the particle's dynamic relaxation time (τ_p) to the fluid's time scale (τ_f):

$$St = \frac{\tau_p}{\tau_f} \tag{13}$$

τ_p: The dynamic relaxation time of particles, measures how quickly particles respond to changes in the fluid flow field.

τ_f: The time scale of the fluid, representing the time available for particle-eddy interactions.

The Stokes number plays a crucial role in determining how turbulence affects particle motion, as highlighted in the studies by Crowe *et al.* [19].

Based on the experimental work of Fessler and Eaton [20], the fluid time scale can be approximated using the following equation:

$$\tau_f = \frac{5H_0}{U_0} \tag{14}$$

It is based on an approximate passing frequency of the large eddy in the separated shear layer. The dynamic relaxation time of particles modified by Fessler and Eaton is as follows.

$$\tau_p = \frac{\rho_p d_p^2}{18\mu\left(1+0.15\,\mathrm{Re}_p^{0.687}\right)} \tag{15}$$

$Re_p$is the average Reynolds number of the particles, which is calculated based on the experimental findings of Fessler and Eaton with a hypothetical average sliding speed of 1.2 m/s. If St << 1, the particle relaxation time is much smaller than the fluid time scale. In this case, particles have sufficient time to respond to changes in fluid velocity, resulting in near-equilibrium between particle and fluid velocities. If St >> 1, the particle relaxation time is much larger than the fluid time scale. Consequently, particles cannot respond effectively to changes in fluid velocity, and their motion remains largely unaffected by the fluid phase.

To study the effects of varying Stokes numbers, copper spheres with diameters of 1, 20, 35, 50, 70, and 100 µm were selected, as listed in Table 4. Each set of spheres was introduced into the flow field after the gas phase simulation reached convergence. The initial velocity of the particles was set equal to the local fluid velocity to ensure dynamic equilibrium between the particles and the gas flow.

Fig. 3 illustrates the trajectories of particles with different Stokes numbers in the backward-facing step flow. The results show that particles with low Stokes numbers closely follow the fluid motion and are strongly influenced by the recirculation zone behind the step.

Table 4. Value of Stokes number according to particle diamete.

Particle material	Copper					
Density	8800					
D (µm)	100	70	50	35	20	1
Stokes number	13.02	5.2	3.7	1.2	0.7	0.0021

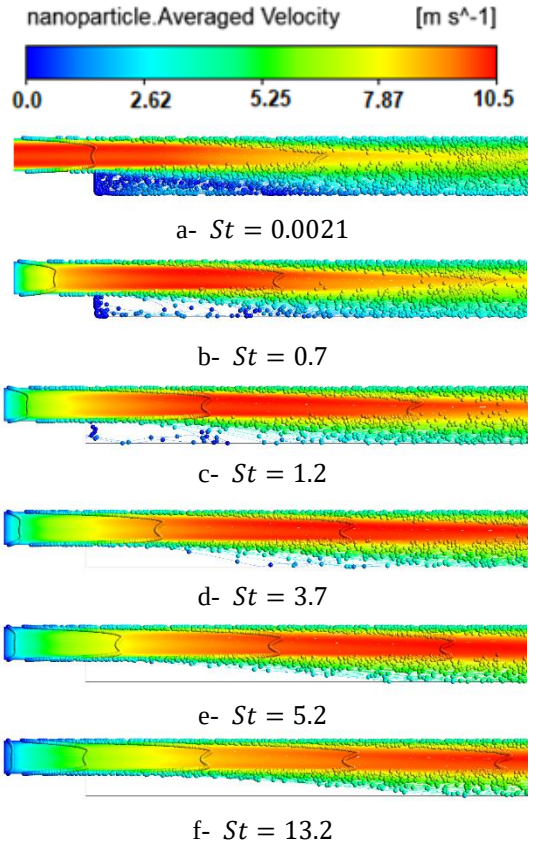

Fig. 3. Particle trajectories for different Stokes numbers in the backward-facing step geometry shown in Fig. 1. The corresponding geometric dimensions are listed in Table 1.

As the Stokes number increases, the particle's response to flow structures decreases, resulting in reduced interaction with the vortex and a tendency to continue along the main flow direction. These observations are consistent with the expected behavior of particle-laden turbulent flows and confirm the capability of the DPM approach to capture particle-vortex interactions. Overall, the results indicate that particle behavior strongly depends on the Stokes number. Particles with low Stokes numbers closely follow the fluid flow, whereas particles with high Stokes numbers exhibit greater inertia and weaker interaction with turbulent structures. As a general result, particles with a very small Stokes number ($St << 1$) are strongly controlled by the eddy structure of the gas phase and closely follow the gas vortices. Such particles cannot be concentrated. Particles with a time scale similar to the time scale of the fluid

$((St \sim O(1)))$ are rotated by a vortex and concentrated along the peripheral region of the vortex. Particles with a large Stokes number $(St >> 1)$ are more stable in maintaining their motion. They cannot respond to eddy motion on the time scale of the existing fluid, nor will they concentrate.

Fig. 4 shows the velocity diagram in the x direction in three sections of the channel with coordinates $x/H = \{2,5,9\}$. In this diagram, the result of Fesler's [20] study can be seen as an experimental result, and the result of Chan *et al.* [21] study can also be seen.

In Table 5, you can see the root mean square error for the data in Fig. 4. As can be seen from the table, the average error for the simulation in the three mentioned coordinates is equal to 0.057. The average error for the data of Chan *et al.* [21] is 0.0627.

In this part of the study, the validity of the DPM method has been investigated, the results of which are shown in Fig. 5. In this method, the equations for the discrete and continuous phases are solved separately, and finally, the discrete phase is related to the continuous phase by the spring term. This solution method requires more calculations and more time. But in the single-phase method, a continuous fluid with new effective properties is defined, which is a function of fluid and nanoparticle properties and volume percentage, and the equations are solved only for a single-phase fluid. Although this method is economical in calculations and time, the accuracy is reduced in exchange for this saving, and the percentage of error increases.

In this problem, for the DPM approach, the maximum speed error is 19%, and for the single-phase method, this error value increases to 25%. In the DPM solution, pressure gradient, virtual mass, and drag forces are active. When the force for Suffman is included in the solution, it is observed that the velocity diagram in the vortex section has a large error and deviates from the experimental process. In the single-phase approach, the effective density of the nanofluid was calculated using the following equation.

$$\rho_{nf} = (1-x)\rho_f + x\rho_p \quad (16)$$

In this equation, ρ_p is the density of the particle (copper), ρ_f is the density of the base fluid (air) and x is the volume fraction equal to 3%.

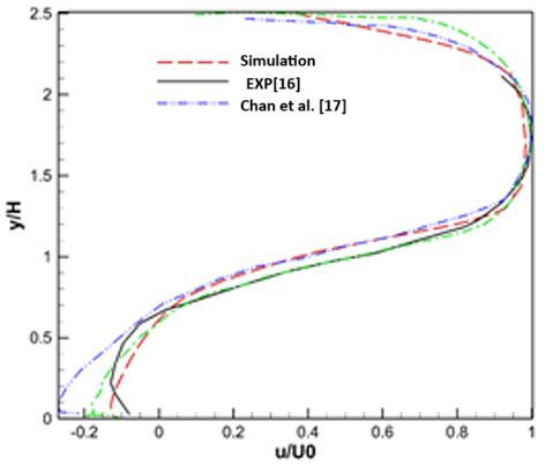

a- $x/H = \{2\}$

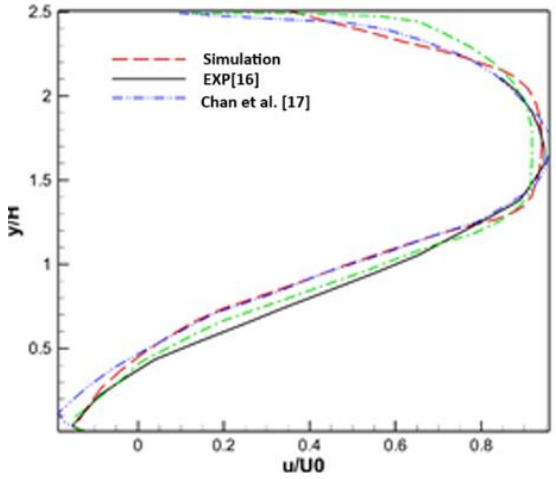

b- $x/H = \{5\}$

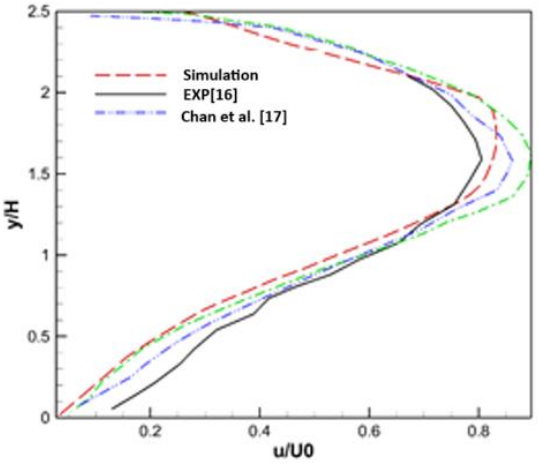

c- $x/H = \{9\}$

Fig.4. Velocity profile in x direction.

Table 5. Root means square error for Fig. 4.

Coordinates	x/H = {9}	x/H = {5}	x/H = {2}
Simulation	0.057926	0.050574	0.065083
Ranut & Enrico	0.037287	0.050099	0.03599
Chan *et al.*	0.062328	0.039394	0.086676

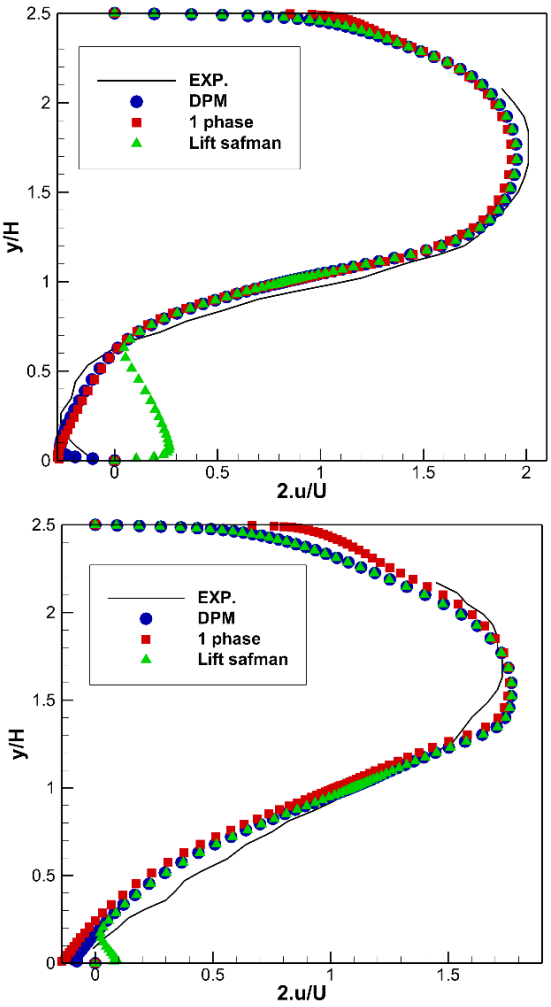

Fig. 5. Comparison of simulation results with two single-phase DPM and Experimental [20] approachesin four sections of the channel with coordinates $x/H = 2\ and\ 7$ according to flow speed.

According to the investigated topics so far, it was observed that the DPM method has less error than the single-phase method. For the particles to enter the eddies, the Stokes number must be much smaller than 1, and according to the density of the desired particle, the diameter of the nanoparticles must be chosen according to the mentioned Stokes number. In the following, using the results obtained in this section, we will examine the addition of nanoparticles in the evaporator shell section.

4. Description of the investigated system and simulation

Fig. 6 shows the air-cooled water HVAC design that was investigated in this part of the study. This example consists of three cycles. First: Refrigeration cycle (main flow), which is shown in the figure with the red line; second: the blue cycle of the evaporator (secondary flow), and its path is indicated by the blue line in the figure; third: the air generator, whose path is the green line, can be seen in the figure.

4.1. Refrigeration cycle

The investigated HVAC system operates based on a conventional vapor-compression refrigeration cycle using R134a as the refrigerant. The cycle consists of a compressor, condenser, expansion valve, and shell-and-tube evaporator, as shown in Fig. 6.

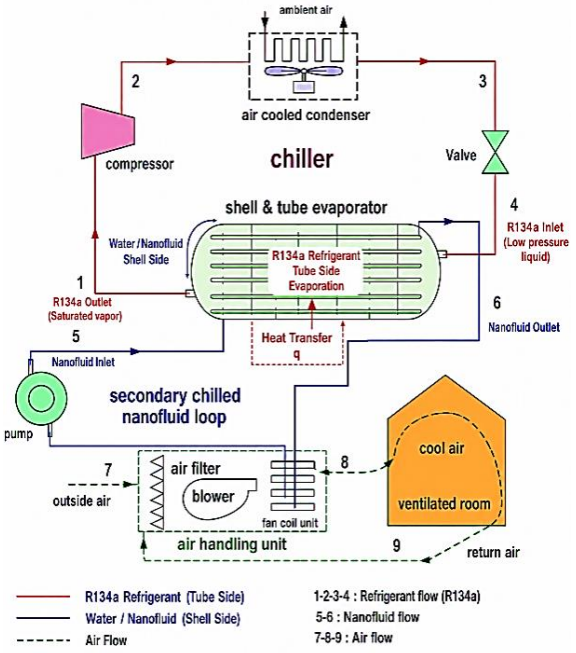

Fig. 6. Schematic representation of the HVAC system and shell-and-tube evaporator, showing the refrigerant (R134a) flow inside the tubes and the secondary fluid (water/nanofluid) flow through the shell side.

Since the primary objective of the present study is to investigate the thermal-hydraulic performance of the evaporator, the remaining components of the refrigeration cycle were not explicitly simulated and are presented only to illustrate the overall system configuration. The numerical analysis is therefore limited to the evaporator and the secondary fluid flowing through its shell side.

4.2. Secondary cycle

The secondary cycle consists of a shell-and-tube evaporator, a fan coil unit, and a circulation pump. Water or nanofluid circulates through this loop and transfers heat to the refrigerant inside the evaporator. After leaving the evaporator, the cooled fluid passes through the fan coil, where it absorbs heat from the conditioned air. The circulation pump compensates for the pressure losses within the loop and maintains the required flow rate. Since the focus of the present study is on the thermal-hydraulic performance of the evaporator, only the evaporator section is considered in the numerical simulations.

4.3. Air conditioner (air handling units (AHUs))

In this section, the ambient air, after passing through the air filter section, is purified and passes through the fan coil with the help of a blower, and its temperature is reduced by indirect heat transfer with the secondary fluid. Then the cool air enters the room and circulates, and enters the air conditioner again as return air. An evaporator is a heat exchanger that is used for two purposes: as an evaporator and a cooling device. In this study, the evaporator was used as an evaporating device. The evaporating evaporator also has different types, of which the tube shell type is the most common and most used. This model is used in two ways. In the first case, the refrigerant passes through the shell side, and the secondary fluid passes through the pipes. In the second case, the flow path of the refrigerant and fluid is changed so that the secondary fluid passes through the shell side and the refrigerant passes through the pipe. In this study, the evaporator has a second state. In the investigated configuration, the refrigerant (R134a) flows inside the tubes and undergoes evaporation, while the secondary fluid (water or nanofluid) flows through the shell side. Heat is transferred from the secondary fluid to the refrigerant through the tube walls, resulting in refrigerant evaporation and cooling of the secondary fluid. Heat transfer is done indirectly with asymmetric flow.

The outer surface of the shell is completely insulated to prevent energy loss. The inlet temperature of the refrigerant is much lower than the temperature of the secondary fluid, and the refrigerant receives heat from the fluid and evaporates during the passage of the pipe path in an isentropic process. In this evaporation process, the temperature is constant, so the temperature of the tube can be considered constant.

The path of the pipes in the converter is one-way and two-way (even or odd). This means that the tube should pass the length of the evaporator only once or several times. It is clear that heat transfer is higher with a larger tube diameter than with the evaporator, but at the same time, the pressure drop is also higher. In this model, a one-way path is used in the evaporator. There are calculations to determine the number of evaporator tubes according to the temperature and pressure of the evaporator and the diameter of the shell, which is omitted in this study. The number of tubes used in this study is 20, with a diameter of 20 mm. There are different layouts for pipes, such as triangular, square, and opposite square, each of which is suitable according to the type of shell fluid and the designer's wishes. For fluids that have the possibility of sedimentation, such as nanofluids, the square arrangement model is suitable because it provides the possibility of better cleaning. That's why this arrangement was used. In evaporators, baffles are used as tube holders and also to increase the fluid path on the shell side. So, the more baffles there are, the more fluid on the shell side passes through the tubes, and as a result, the amount of turbulence of the fluid increases and, as a result, the heat transfer increases. Besides the benefit of increasing heat transfer in the evaporator, baffles also cause a pressure drop and increase the pump's work. For this reason, they have introduced an optimal

interval for the distance of the baffles in relation to the diameter of the shell. The number of baffles examined is in models 3, 5, and 7. Another thing that is very important in baffles is the amount of baffle plate cut, the best size of which is 25%, which is also included in this study.

4.4. Modeling and boundary conditions

Three evaporator models with 3, 5, and 7 baffles were investigated symmetrically in this study, which are shown in Figs. 7-9, respectively, and a converter with 7 and 5 baffles. This system is modeled using the laws of conservation of energy, mass, and momentum. Key dimensions and parameters are presented in Table 6.
The field is modeled in a three-dimensional and axially symmetrical manner and is meshed in the form of an organized triangular mesh. Cells are smaller near the tubes and baffles. The boundary layer mesh is used for the tube wall, baffle and shell, and y^+ is less than 1. In Fig. 9, you can see the meshing.

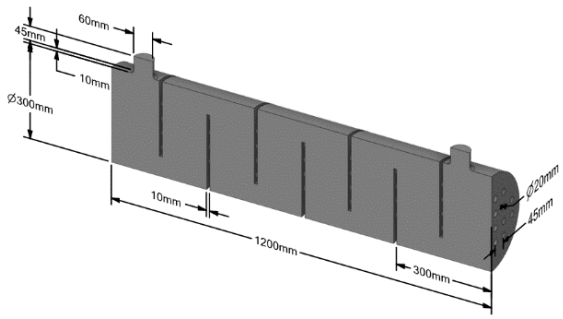

Fig. 7. Evaporator model with 7 baffles.

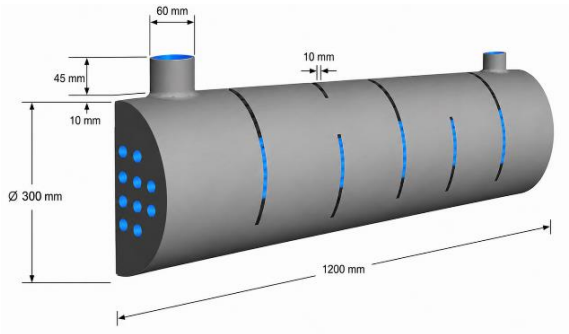

Fig. 8. Evaporator model with 5 baffles.

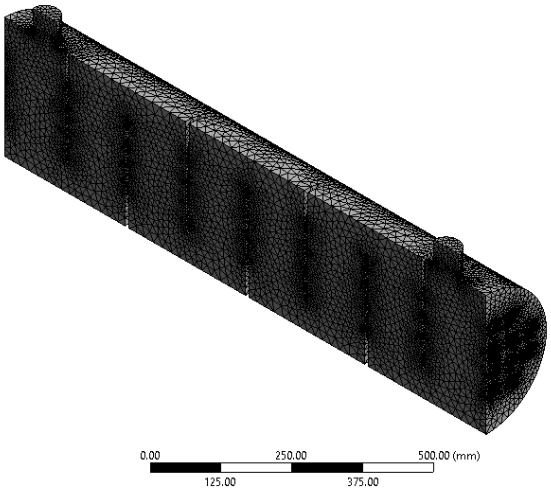

Fig.9. Evaporator converter network with 7 baffles.

Table 6. Specifications of the evaporator.

Parameter	Quantity
Diameter pipe	20 mm
Length of the pipe	1200 mm
Number of tubes	20
Pipe spacing	45 mm
Number of baffles	5-7
Baffle cut	25%
Shell diameter	300 mm

For clarity and reproducibility, the numerical setup adopted in the present study is summarized in Table 7. The table provides the main solver settings, turbulence model, discretization schemes, convergence criterion, and DPM configuration used in the simulations.
The numerical simulations were considered converged when the residuals of the governing equations decreased below 10^{-6}.

Table 7. Numerical solver settings.

Parameter	Value
Software	ANSYS Fluent 2021
Flow model	Three-dimensional
Continuous phase	Steady
Particle tracking	Transient DPM
Turbulence model	SST k-w
Pressure-velocity coupling	Coupled
Momentum discretization	Second-order
Energy discretization	Second-order
Turbulence coupling	Two-way coupling
Convergence criterion	Residuals below 10^{-6}
Selected mesh	574954 cells
Symmetry condition	Applied

In addition, key monitored variables such as the outlet temperature and overall heat transfer coefficient remained unchanged with further iterations, indicating convergence of the numerical solution.

The evaporator configuration with five baffles was selected based on conventional shell-side design considerations. A smaller number of baffles may provide insufficient flow disturbance and mixing, while an excessive number of baffles can promote recirculation zones, stagnant regions, and additional pressure losses. Therefore, five baffles were considered as a representative and practical configuration for the present study.

The independence of the simulation results from the mesh was checked. To check the independence of the network for three meshes, the water outlet temperature for the evaporator with 7 baffles is given in Table 8. The selected mesh for solving has 574954 cells. For the evaporators with 5 and 3 baffles, the independence of the results from the grid was checked in the same way.

The numerical simulations were performed using ANSYS Fluent 2021 and ANSYS CFX 2021. Preliminary investigations and verification studies were conducted using both solvers. However, all results presented in this manuscript were obtained using the Eulerian-Lagrangian Discrete Phase Model (DPM) implemented in ANSYS Fluent 2021. The equations were solved with second-order accuracy and with the Eulerian-Lagrangian approach. The flow is simulated in a stable and three-dimensional mode. To model the flow turbulence, the SST k-ω turbulence model was chosen. For the convergence of the nanofluid flow solution, the base fluid or water has been simulated stably, and the particles transiently. In order to save time and calculations due to the symmetry of the geometry, the problem has been investigated in a symmetry-oriented way. The standard mode was used to solve the pressure equations, and the pressure and velocity equations were coupled. The problem is modeled in two ways, and the momentum and energy equations are solved with the second order. Among the forces available in the Eulerian-Lagrangian method, the virtual mass force and the pressure gradient are used to investigate the turbulence in the solution; the two-way turbulence coupling option was given in the solution. The spherical model was used for post law.

In this model, the water passes through the shell, and the refrigerant inside the tube is changing phase. Therefore, the temperature of the evaporator was considered constant. In the investigated evaporator, the refrigerant flows inside the tubes and undergoes a phase change during evaporation. Since the evaporation process occurs approximately at a constant saturation temperature, the tube wall temperature was assumed to be constant in the numerical model. Therefore, instead of directly simulating the two-phase refrigerant flow, the tube-side evaporation process was represented by a constant wall temperature boundary condition. This assumption enables the study to focus on the thermal-hydraulic behavior of the shell-side secondary fluid and the influence of nanoparticle dispersion on heat transfer performance. The applied boundary condition is given in Table 9.

To provide a clearer description of the numerical model, the main specifications of the shell-and-tube evaporator, thermophysical characteristics of the working fluids, and operating conditions employed in the simulations are summarized in Table 10. The listed parameters were used throughout the computational analysis and parametric investigations.

Table 8. Independence from meshing.

Number of cells	Water outlet temperature	Percentage of changes
452791	276.225	
574954	276.145	0.028 %
666235	276.139	0.0021 %

Table 9. Boundary condition.

Boundary	Variable	Unit	Quantity
Inlet	Secondary flow temperature	k	310-285
Inlet	Secondary flow mass flow rate	kg/s	24-1
Inlet	Evaporator temperature	k	233-272
Inlet	Particle diameter	nm	10
Inlet	Volume fraction	-	0.06-0
Outlet	$\overline{P}$	Pa	0
Wall	$\bar{u}$	m/s	(0 0 0)
Wall	$\dot{q}$	W/m^2	0

Table 10. Heat exchanger and working fluid specifications.

Parameter	Value
Heat exchanger type	Shell-and-tube evaporator
Working fluid (Shell side)	Water / Nanofluid
Nanoparticles	Al_2O_3, Al_2O_3–TiO_2
Nanoparticle diameter	10 nm
Volume fraction tange	0–0.06
Inlet temperature tange	285–310 K
Evaporator temperature range	233–272 K
Mass flow rate range	1–24 kg/s
Number of baffles	3, 5, 7
Numerical approach	Eulerian-Lagrangian DPM
Turbulence model	SST k-ω

This study evaluates the performance of 3 different fluids. Water has been used as the base fluid and the comparison of its performance with Al_2O_3 and TiO_2 nanoparticles in the base fluid has also been investigated. The properties of nanoparticles and water can be seen in Table 11.

4.5. Result discussion

Fig. 10 shows the temperature distribution for the base fluid at the inlet temperature of 12°C and the evaporator temperature of -10°C for the evaporator with 5 baffles.

Fig. 11 shows the path of the particles for the evaporator with 5 baffles. The particles shown in solid blue color are for the initial time of the injection, and as it fades, it shows the progress of the particles in terms of time. As can be seen in the figure, most of the particles travel the length of the evaporator and exit it in the first 30 seconds. The particles that are seen in green enter the vortices after each baffle and are still present in the vortices until 60 seconds, and after that, they gradually leave the vortices. Particles that are still involved in vortices after 90 seconds are seen in yellow in the figure.

Fig. 12 shows the temperature changes during the passage through the evaporator for the condition of inlet temperature of 12 and evaporator temperature of -10 degrees Celsius. The temperature of the particles decreases along the way, and also, the particles that are in the vortices behind the baffle have a lower temperature than the adjacent particles outside the vortex.

Table 11. Thermophysical properties of nanoparticles and water.

Material	Density Kg m^{-3}	Specific heat coefficient J kg^{-1} K^{-1}	Heat conduction W m^{-1} K^{-1}
Al_2O_3	3970	765	36
TiO_2	4157	710	8.4
Water	997	4181.7	0.6069

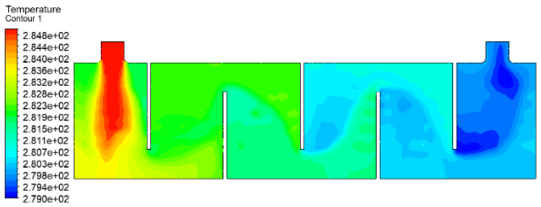

Fig. 10. Temperature distribution for nanofluid at inlet temperature of 12°C and evaporator temperature of -10°C for evaporator with 5 baffles.

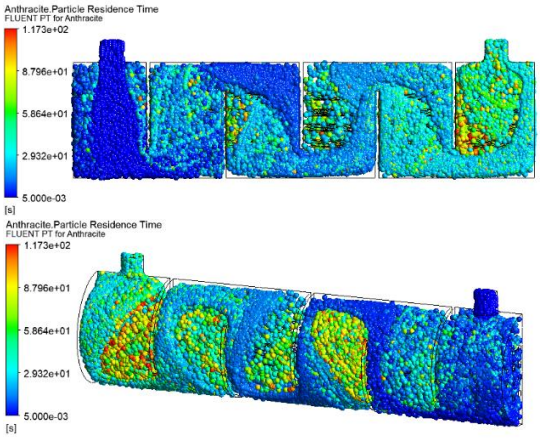

Fig. 11. Path of nanoparticles at inlet temperature of 17°C and evaporator temperature of -10°C for evaporator with 5 baffles.

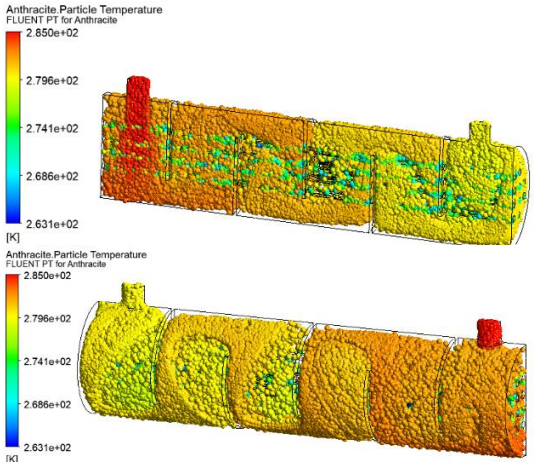

Fig. 12. Nanoparticle temperature change along the way for the conditions of inlet temperature 12 and evaporator temperature -10 degrees Celsius.

The particles that are close to the tubes have the lowest temperature due to heat transfer with the tubes.

Fig. 13 shows the path of hybrid nanoparticles for the evaporator with 5 baffles. Al_2O_3 particles are shown with red spheres and TiO_2 with blue spheres. The dispersion of hybrid particles is greater than that of single nanoparticles. The paths of different types of particles, which are shown with two different colors, are different in many parts of the geometry, which can be attributed to the difference in the density of different particles. One of the reasons for the improvement of heat transfer when using hybrid nanoparticles can be considered to be the different path and greater dispersion of particles in the fluid.

The overall heat transfer coefficient in the evaporator is an important factor in determining the cooling effect of the HVAC unit. This factor calculates the heat transfer coefficient in the evaporator tube and shell. As seen in the equations, this parameter is a function of the properties of the working fluids on both sides of the evaporator heat exchanger, the working-fluid mass flow rate, and the dimensions of the heat-transfer surface in the evaporator. Since the working fluid (R134a) flowing on the tube side of the evaporator is the same for all secondary fluids considered, the value of h_i on the tube side will be the same for all working fluids considered on the shell side.

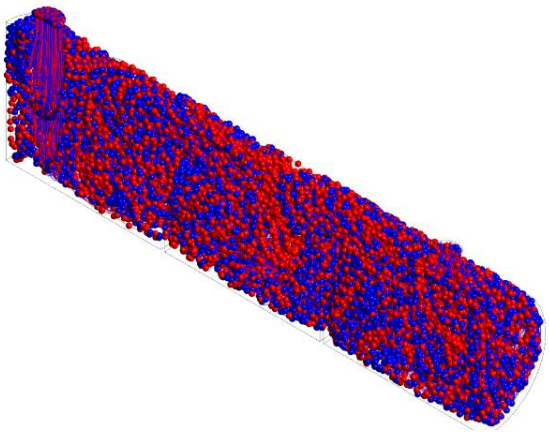

Fig. 13. Path of hybrid nanoparticles at inlet temperature of 12°C and evaporator temperature of -10°C for evaporator with 5 baffles.

The effect of using nanoparticles in water is shown in Fig. 14 in terms of fluid inlet temperature between 285 and 310 K in two Eulerian-Lagrangian and mixed single-phase modes for a converter with 5 baffles. For the exchanger with 5 baffles, the overall heat transfer coefficient increases with the increase in the inlet temperature of the secondary fluid. From the figure, it can be seen that with the Eulerian-Lagrangian approach, by adding nanoparticles to the base fluid, the overall heat transfer coefficient increases by about 5.8%. From Fig. 14, it can be seen that, using the Eulerian-Lagrangian approach, the addition of nanoparticles to the base fluid increases the overall heat transfer coefficient by approximately 5.8%. For the same conditions, the single-phase model predicts an enhancement of about 9.8%. The comparison between the two approaches reveals a significant relative difference of approximately 68% in the predicted heat transfer enhancement. This observation indicates that particle transport and dispersion effects have a considerable influence on the thermal performance prediction. Therefore, the DPM approach was adopted in the present study because it allows separate tracking of nanoparticles and provides a more detailed representation of nanofluid behavior.

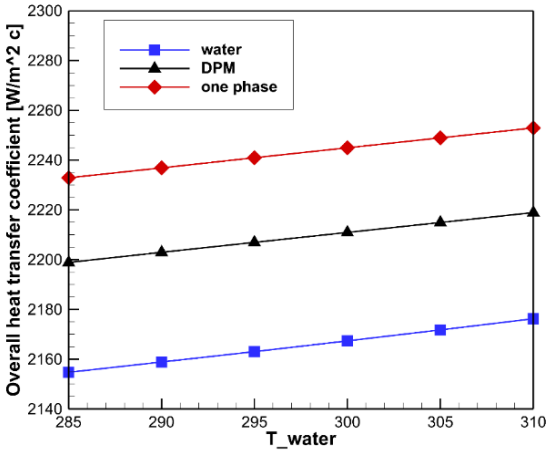

Fig. 14. The diagram of the overall heat transfer coefficient according to the temperature of the secondary fluid entering for the Al_2O_3 particle with two DPM approaches and single phase for a converter with 5 baffles, with a tube temperature of 263 K and a volume fraction of 5.5%.

The enhancement in the overall heat transfer coefficient can be attributed to the higher thermal conductivity of Al_2O_3 nanoparticles compared with the base fluid. The suspended nanoparticles improve thermal energy transport within the fluid and promote a more uniform temperature distribution. In addition, particle-fluid interactions and local mixing mechanisms contribute to reducing thermal resistance near the heat transfer surfaces. Similar behavior has been reported by Ahmed *et al.* [6] and Bhattad *et al.* [4], who observed that the addition of nanoparticles improves heat transfer performance in refrigeration and cooling systems.

In Fig.15, the effect of using mono and hybrid nanoparticles was investigated by the Eulerian-Lagrangian method for a converter with 7 baffles and an evaporator temperature of 263 and a volume fraction of 5.5% based on the temperature of the secondary fluid. As is evident from the graph, hybrid particles increase the overall heat transfer coefficient more than mono particles, which reaches 8.8% for hybrid particles.

The superior performance of the hybrid nanofluid can be explained by the combined thermophysical characteristics of Al_2O_3 and TiO_2 nanoparticles. The presence of particles with different densities and thermal conductivities leads to improved particle dispersion and enhanced energy transport within the fluid. As observed in Fig. 13, the trajectories of the hybrid nanoparticles are more widely distributed throughout the flow domain, which increases the probability of thermal interaction and contributes to the higher overall heat transfer coefficient. By increasing the number of baffles, the overall heat transfer coefficient for both water fluid and nanofluid has increased by about 12.74%.

Fig. 16 shows the graph of the overall heat transfer coefficient for the evaporator temperature for the converter with 3, 5, and 7 baffles and a fixed inlet temperature of 285 K and a volume fraction of 5.5%. As the evaporator temperature decreases, the overall heat transfer coefficient increases for all models. At a temperature close to zero, the difference in the value of the overall heat transfer coefficient increases for the models with 5 and 3 baffles. Based on the results, the more baffles there are, the more the overall heat transfer coefficient increases due to the creation of more back-and-forth paths in the secondary fluid and also the turbulence of the flow. But this increase in the number of baffles increases the pressure drop in the shell.

Increasing the number of baffles intensifies flow redirection and promotes stronger recirculation zones within the shell side. The resulting increase in turbulence enhances fluid mixing and reduces the thermal boundary layer thickness around the tubes, leading to higher heat transfer coefficients.

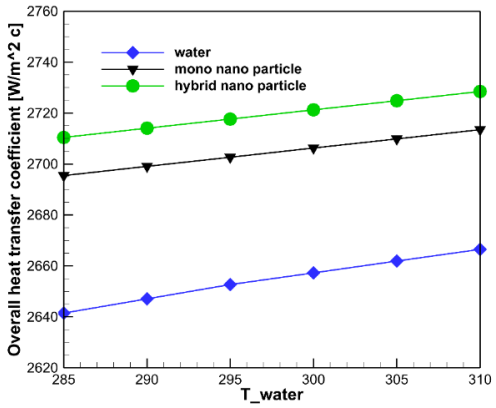

Fig. 15. The diagram of the overall heat transfer coefficient according to the temperature of the secondary fluid entering for Al_2O_3, Al_2O_3+TiO_2 particles with the DPM approach for a converter with 7 baffles with a tube temperature of 263 K and a volume fraction of 5.5%.

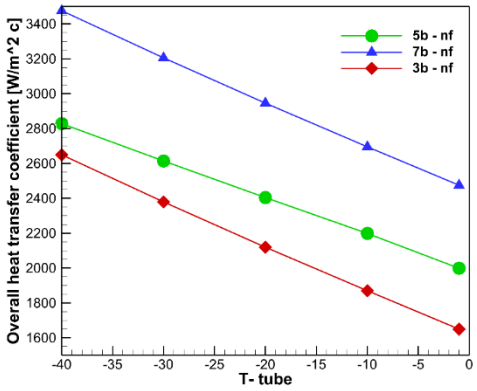

Fig. 16. Diagram of overall heat transfer coefficient according to evaporator temperature for Al_2O_3 particle with DPM approach for converter with 3, 5, and 7 baffles with inlet temperature of 285 K and volume fraction of 5.5%.

However, this improvement is accompanied by an increase in pressure drop, indicating the existence of a trade-off between thermal enhancement and pumping power requirements. To determine the range of the volume fraction of particles that due to the addition of nanoparticles, the increase in heat transfer will be greater than the increase in the work of the evaporator pump (due to the greater pressure drop caused by the addition of particles), the PEC ratio, which is equal to the ratio of the heat transfer to the work of the pump Evaporator is introduced. In addition to heat transfer enhancement, the hydraulic performance of the shell-side flow was also considered. The pressure drop was obtained from the difference between the area-averaged static pressures at the shell-side inlet and outlet. These pressure-drop values were subsequently used in the calculation of the performance evaluation criterion (PEC), allowing simultaneous assessment of thermal enhancement and the corresponding hydraulic penalty associated with nanoparticle addition. Fig. 17 shows the PEC $_{nf}$/ PEC $_{bf}$ ratio in terms of nanoparticle volume percentage for the Al_2O_3 particle and the model with 5 baffles. Based on these results, for this sample, the volume fraction interval up to 0.03 has been shown as the optimal interval where the amount of heat transfer is greater than the pressure drop. And its maximum value for volume fraction is 0.02. For a volume fraction of more than 0.03, the increase in the work of the evaporator pump is more than the increase in heat transfer, and for this reason, adding more particles is not cost-effective.

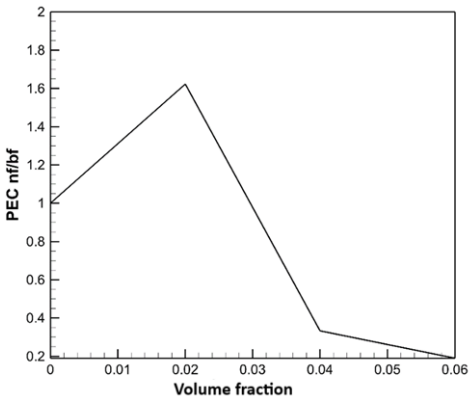

Fig. 17. PEC $_{nf}$/ PEC $_{bf}$ ratio diagram in terms of nanoparticle volume percentage for Al_2O_3 particle and model with 5 baffles.

Fig. 18 shows the change of the overall heat transfer coefficient in terms of the mass flow rate of the secondary fluid. With the increase in mass flow rate, the overall heat transfer coefficient increases, but the slope of this increase is higher for the converter with 7 baffles than for the converter with 5 baffles. For a mass flow rate close to 1, the value of the overall heat transfer coefficient for the two geometries is very close, and with the increase in the mass flow rate, the difference between these two values increases significantly.

4.6. Limitations of the present study

The present study provides a detailed numerical investigation of nanofluid behavior in a shell-and-tube chiller evaporator using the Eulerian-Lagrangian DPM approach. However, several limitations should be acknowledged. First, the refrigerant-side flow and phase-change process were not directly simulated. Instead, the evaporation process was represented using a constant wall temperature boundary condition. Second, a fixed nanoparticle diameter was considered throughout the simulations. Third, particle agglomeration, sedimentation, and possible changes in thermophysical properties due to long-term operation were neglected. In addition, the numerical results were not validated against experimental data for the investigated evaporator geometry.

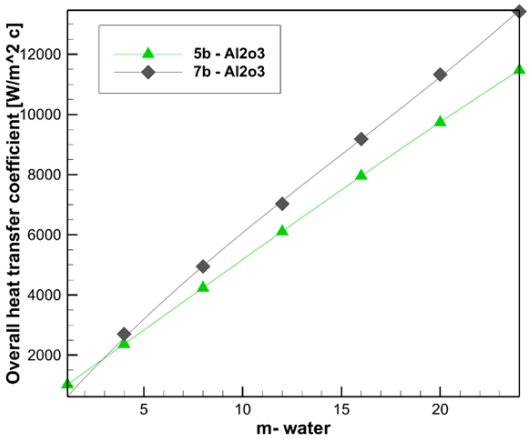

Fig. 18. Graph of overall heat transfer coefficient in terms of mass flow rate of secondary fluid for two models with 5 and 7 baffles for nanofluid with volume fraction of 5.5%.

Future studies may incorporate detailed refrigerant boiling models, particle agglomeration mechanisms, and experimental validation to further improve the accuracy of the predictions.

5. Conclusions

Increasing the number of baffles enhanced the overall heat transfer coefficient. In the investigated evaporator, increasing the number of baffles from 5 to 7 resulted in a 6.94% increase in the overall heat transfer coefficient. Furthermore, the addition of Al_2O_3 nanoparticles to the base fluid improved the heat transfer coefficient by 5.8%, while the use of Al_2O_3–TiO_2 hybrid nanoparticles increased this enhancement to 8.8%.

Although the Eulerian-Lagrangian Discrete Phase Model (DPM) requires greater computational effort than the conventional single-phase approach due to the separate solution of fluid and particle equations, it provides a more detailed representation of nanoparticle transport, dispersion, and interaction with the flow field. A comparison between the DPM and single-phase approaches revealed a relative difference of approximately 68% in the predicted thermal performance, highlighting the importance of considering particle dynamics in numerical simulations of nanofluids. Therefore, the DPM approach is recommended for obtaining more realistic predictions of nanofluid behavior in shell-and-tube evaporators.

6. References

[1] A. Bhattad, J. Sarkar, and P. Ghosh, "Discrete phase numerical model and experimental study of hybrid nanofluid heat transfer and pressure drop in plate heat exchanger," *Int. Commun. Heat Mass Transf.*, Vol. 91, pp. 262–273, (2018).

[2] S. Rahman, S. Issa, Z. Said, M. E. H. Assad, R. Zadeh, and Y. Barani, "Performance enhancement of a solar powered air conditioning system using passive techniques and SWCNT/R-407c nano refrigerant," *Case Stud. Therm. Eng.*, Vol. 16, p. 100565, (2019).

[3] N. Jeyakumar, C. Uthranarayan, and B. Narayanasamy, "Energy conservation in the refrigeration system through improvement of Coefficient of Performance and power consumption reduction using Nanofluids," *Int. J. Ambient Energy*, Vol. 43, No. 1, pp. 1120–1126, (2022).

[4] A. Bhattad, J. Sarkar, and P. Ghosh, "Improving the performance of refrigeration systems by using nanofluids: A comprehensive review," *Renew. Sustain. Energy Rev.*, Vol. 82, pp. 3656–3669, (2018).

[5] A. A. Vasconcelos, A. O. C. Gómez, E. P. Bandarra Filho, and J. A. R. Parise, "Experimental evaluation of SWCNT-water nanofluid as a secondary fluid in a refrigeration system," *Appl. Therm. Eng.*, Vol. 111, pp. 1487–1492, (2017).

[6] M. S. Ahmed and A. M. Elsaid, "Effect of hybrid and single nanofluids on the performance characteristics of chilled water air conditioning system," *Appl. Therm. Eng.*, Vol. 163, p. 114398, (2019).

[7] M. S. Ahmed, M. R. A. Hady, and G. Abdallah, "Experimental investigation on the performance of chilled-water air conditioning unit using alumina nanofluids," *Therm. Sci. Eng. Prog.*, Vol. 5, pp. 589–596, (2018).

[8] N. Monirimanesh, S. M. Nowee, S. Khayyami, and I. Abrishamchi, "Performance enhancement of an experimental air conditioning system by using TiO2/methanol nanofluid in heat pipe heat exchangers," *Heat and Mass Trans.*, Vol. 52, pp. 1025–1035, (2016).

[9] N. Balaji, P. S. M. Kumar, R. Velraj, and N. Kulasekharan, "Experimental investigations on the improvement of an air conditioning system with a nanofluid-based intercooler," *Arab. J. Sci. Eng.*, Vol. 40, pp. 1681–1693, (2015).

[10] E. Firouzfar, M. Soltanieh, S. H. Noie, and S. H. Saidi, "Energy saving in HVAC systems using nanofluid," *Appl. Therm. Eng.*, Vol. 31, No. 8–9, pp. 1543–1545, (2011).

[11] O. A. Alawi, N. A. C. Sidik, and others, "Applications of nanorefrigerant and nanolubricants in refrigeration, air-conditioning and heat pump systems: A review," *Int. Comm. in Heat and Mass Trans.*, Vol. 68, pp. 91–97, (2015).

[12] M. M. Myat, S. Thu, and T. N. Aung, "A comprehensive review of nanofluids in HVAC&R systems: Applications, performance enhancement and nges,"

Sustainability, Vol. 17, No. 16, pp. 7371, (2025).

[13] S. Kalsi, A. Kumar, and R. Singh, "A review on hybrid nanofluids for heat transfer: Advancements, synthesis, challenges and applications," *Discover Applied Sciences*, Vol. 7, No. 698, pp. 1-21, (2025).

[14] M. R. Aliyu, M. A. Hamza, and A. Ibrahim, "Performance improvement of an HVAC system using water-based hybrid nanofluids," *PLoS One*, Vol. 20, No. 5, pp. 1-24, (2025).

[15] N. Ali, A. Basem, P. Ghodratallah, P.K. Si ngh, A. Musa, J. Jasim, R.Ali, H. Rajab, M. Ahmed and A.A. Alizad, "Eulerian-Lagrangian numerical investigation of the fluid flow properties and heat transfer of a nanofluid-cooled micro pin-fin heat sink," *J. Taiwan Inst. Chem. Eng*., Vol. 164, pp. 105674, (2024).

[16] S. Goutam and M. C. Paul, "Discrete phase approach for nanofluids flow in pipe," in *Proc. 2nd Int. Conf. on Advances in Civil, Structural and Mechanical Engineering (CSM)*, Birmingham, UK, 2014, pp. 99–103.

[17] R. D. Selvakumar and S. Dhinakaran, "Heat transfer and particle migration in nanofluid flow around a circular bluff body using a two-way coupled Eulerian-Lagrangian approach," *Int. J. Heat Mass Transf.*, Vol. 115, pp. 282–293, (2017).

[18] M. Bovand, S. Rashidi, G. Ahmadi, and J. A. Esfahani, "Effects of trap and reflect particle boundary conditions on particle transport and convective heat transfer for duct flow-A two-way coupling of Eulerian-Lagrangian model," *Appl. Therm. Eng.*, Vol. 108, pp. 368–377, (2016).

[19] C. T. Crowe, J. N. Chung, and T. R. Troutt, "Particle mixing in free shear flows," *Prog. Energy Combust Sci.*, Vol. 14, No. 3, pp. 171–194, (1988).

[20] J. R. Fessler and J. K. Eaton, "Turbulence modification by particles in a backward-facing step flow," *J. Fluid Mech.*, Vol. 394, pp. 97–117, (1999).

[21] C. K. Chan, H. Q. Zhang, and K. S. Lau, "Numerical simulation of gas-particle flows behind a backward-facing step using an improved stochastic separated flow model," *Comput. Mech.*, Vol. 27, No. 5, pp. 412–417, (2001).